Ultrasound focusing images in superlattices

Michiko Narita, Yukihiro Tanaka and Shin-ichiro Tamura

Department of Applied Physics, Hokkaido University, Sapporo 060, Japan

Abstract
We study theoretically ultrasound focusing in periodic multilayered structures,
or superlattices, by solving the wave equation with the Green function
method and calculating the transmitted ultrasound amplitude images of both
the longitudinal and transverse modes. The constituent layers assumed are
elastically isotropic but the periodically stacked structure is anisotropic. Thus
anisotropy of ultrasound propagation is predicted even at low frequencies and
it is enhanced significantly at higher frequencies due to the zone-folding effect
of acoustic dispersion relations. An additional effect studied is the interference
of ultrasound (known as the internal diffraction), which can be recognized
when the propagation distance is comparable to the ultrasound wavelength.
Numerical examples are developed for millimetre-scale Al/polymer multilayers
used recently for imaging experiment with surface acoustic waves.

(Some figures in this article are in colour only in the electronic version)

1. Introduction

The ballistic energy transport associated with lattice vibrations is governed by the group
velocity of acoustic phonons and is highly anisotropic in crystalline solids [1–3]. In synthetic
superlattices Brillouin-zone folding due to macroscopic periodicity along the growth direction
considerably modifies the phonon dispersion relations from those in bulk crystals [4–9]. As
a result, phonon group velocities and the resulting acoustic energy transport are expected to
be highly frequency dependent and to exhibit quite different characteristics from those in bulk
solids. Anomalous reductions of lattice thermal conductivity in semiconducting superlattices
observed recently [10–12] are believed to relate to this modification of the phonon group
velocity in multilayered structures [13–15].

Tanaka *et al* [16] have recently studied anisotropic phonon propagation or phonon focusing
in superlattices with geometrical acoustic approximation (the ray picture for phonons). They
have shown that the existence of zone-centre, zone-edge and internal gaps in the mini
Brillouin zone of a superlattice causes considerable deformation of the constant-frequency
surfaces of phonons, leading to the appearance and disappearance of phonon caustics for
both the longitudinal and transverse modes. Here we note that the phonon focusing effect has

traditionally been studied by heat-pulse experiments involving high-frequency non-equilibrium acoustic phonons in the frequency range 100–1000 GHz (the corresponding temperatures are 5–50 K and wavelengths are 1–10 nm) with bulk samples of thickness ∼1–10 mm. Thus, the sample dimension is much larger than the phonon wavelength and the geometrical acoustic approximation holds for the ballistically propagating phonons. The thicknesses of conventional semiconductor superlattices are very small (typically in the range of 1 μm) but the geometrical acoustic approximation is still valid for those high-frequency phonons. However, it would not be so easy for a heat-pulse experiment to resolve the spatial distribution of the energy flux propagating inside these superlattices.

Thus, for the experimental study of phonon focusing in superlattices it is desirable to use a sample of dimensions ∼1–10 mm and this means that the unit period of the superlattice is also in the millimetre or submillimetre range. In addition, to observe the effects characteristic of the superlattice, i.e. the zone-folding effects, the bilayer thickness has to compete with the wavelength of the phonons. For a superlattice with the layer thickness in the millimetre range, the lowest Bragg frequency is decreased to several MHz, which can be probed by ultrasound rather than high-frequency phonons [17, 18].

After the publication of [16], an imaging experiment of surface acoustic waves propagating on Al/polymer multilayers (the surface is parallel to the layer normal) was reported by Vines *et al* [19]. In their experiment with immersion transducers the bilayer thickness of the sample is 1 mm (the thickness of the superlattice sample is 2 cm) and the frequencies generated are 1–10 MHz. Extension of this experiment to a transmission experiment studying bulk ultrasound focusing in multilayered structures should be straightforward.

Here we note that at a frequency of 1 MHz the corresponding wavelength λ becomes $\lambda \simeq 3$ mm, which is not negligible compared with the sample dimensions. Hence, we expect that the features characteristic of the wave acoustics will be observed in the ultrasound images of this frequency range. A bulk focusing experiment at frequencies of several MHz has been done by Hauser *et al* [17, 18] with an ultrasound beam emitted from a coherently driven point source. The existence of interference fringes in the image is observed in the high-intensity regions where the high-frequency phonons are expected to focus strongly due to the folding of the group-velocity surface. (The interference occurs by the overlapping of acoustic fields with different wavevectors in a given group-velocity direction.) This self-interference due to elastic anisotropy is called 'internal diffraction' [17, 18]. Our analysis will also elucidate the finite-wavelength effect, or internal diffraction, on ballistic phonon (ultrasound) propagation in periodic superlattices.

Another interesting aspect of the experiment by Vines *et al* [19] is the fact that the constituent materials of the superlattice, i.e. polycrystalline aluminium and polymer, are both isotropic elastically. However, the anisotropic phonon or ultrasound propagation should be observed because of the presence of the anisotropy associated with the one-dimensional layering structure of the superlattice. This anisotropy will manifest itself in bulk ultrasound images even at frequencies much smaller than the zone-boundary values. In the analysis of [16] both constituent materials of the superlattice are highly anisotropic elastically, so it is hard to recognize (especially at low frequencies) the anisotropy associated with the periodically stacked structure alone. In the present work we are also able to show, through the study of the ultrasound images, the effects on the phonon focusing purely caused by the anisotropy associated with the composite layering structure, which is enhanced at high frequencies by zone-folding effects.

It should be noted that in the ultrasound imaging experiment (see [17–19]), the displacement amplitude perpendicular to the sample surface opposite the excitation surface is usually measured. Thus, the polarization vectors of the ultrasound transmitted through the
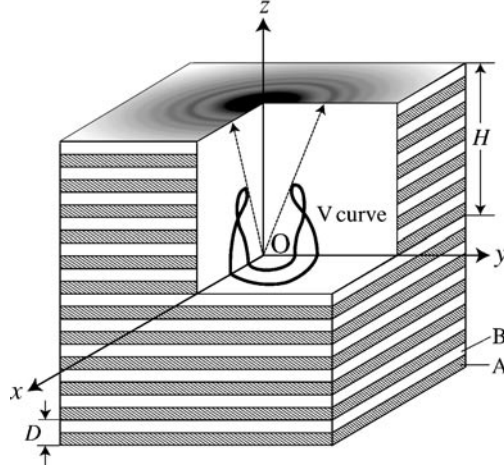
Figure 1. A schematic of a periodic superlattice consisting of alternate A and B layers. The layer interfaces are parallel to the x–y plane and the growth direction is parallel to the z-axis. The full curves in the x–y, y–z and z–x sections illustrate the group-velocity curves of the slow transverse phonons (corresponding to those in figure 4(b) below) and the dashed lines with arrows indicate caustic directions. The phonon image on the x–y plane is shown schematically.

superlattice play important roles. This implies that an analysis based only on the constant-frequency and the resulting group-velocity surfaces (that was made in [16]) is not sufficient for analysing phonon focusing at ultrasound frequencies. We have to solve the inhomogeneous wave equation in the presence of the external point source and determine the displacement amplitude of the ultrasound transmitted through the periodic superlattice. For this purpose we will develope a new formulation based on the Green function method where the lattice Green tensor is expanded in terms of the complete orthogonal set of eigenfunctions of the perfect, periodic system with the help of Fourier expansion of the eigenvectors satisfying the Bloch theorem.

2. Formulation

We consider a perfect superlattice consisting of an infinite repetition of alternating layers of materials A (with thickness d_A, mass density ρ_A and elastic stiffness tensor $c_{ijmn,A}$) and B (with thickness d_B, mass density ρ_B and elastic stiffness tensor $c_{ijmn,B}$). The interfaces are parallel to the $\boldsymbol{x}_\parallel = (x, y) = (x_1, x_2)$ plane, with the z-axis (x_3-axis) normal to the interfaces (see figure 1).

The equation governing the motion of lattice displacement $\boldsymbol{u}(\boldsymbol{r}, t)$ of the system under the external harmonic force $\boldsymbol{f} = \boldsymbol{f}(\boldsymbol{r}, t)$ is given by

$$\rho(z)\ddot{u}_i = \partial_j[c_{ijmn}(z)\partial_n u_m] + f_i$$
$$\equiv \hat{L}_{ij}u_j + f_i \qquad (i = 1, 2, 3) \tag{1}$$

where $\boldsymbol{r} = (\boldsymbol{x}_\parallel, z)$, $\rho(z)$ and $c_{ijmn}(z)$ are the position-dependent mass density and elastic stiffness tensor (which take either ρ_A and $c_{ijmn,A}$, or ρ_B and $c_{ijmn,B}$ depending on z), and the summation convention over repeated indices is assumed. Explicitly, the tensor operator $\hat{L}$ is

given by

$$
\hat{L} =
\begin{bmatrix}
C_{11}\frac{\partial^2}{\partial x^2} + C_{44}\frac{\partial^2}{\partial y^2} + \frac{\partial}{\partial z}C_{44}\frac{\partial}{\partial z} & (C_{12}+C_{44})\frac{\partial^2}{\partial x\partial y} & C_{12}\frac{\partial^2}{\partial x\partial z} + \frac{\partial}{\partial z}C_{44}\frac{\partial}{\partial x} \\
(C_{44}+C_{12})\frac{\partial^2}{\partial x\partial y} & C_{44}\frac{\partial^2}{\partial x^2} + C_{11}\frac{\partial^2}{\partial y^2} + \frac{\partial}{\partial z}C_{44}\frac{\partial}{\partial z} & C_{12}\frac{\partial^2}{\partial y\partial z} + \frac{\partial}{\partial z}C_{44}\frac{\partial}{\partial y} \\
C_{44}\frac{\partial^2}{\partial x\partial z} + \frac{\partial}{\partial z}C_{12}\frac{\partial}{\partial x} & C_{44}\frac{\partial^2}{\partial y\partial z} + \frac{\partial}{\partial z}C_{12}\frac{\partial}{\partial y} & C_{44}\left(\frac{\partial^2}{\partial x^2}+\frac{\partial^2}{\partial y^2}\right) + \frac{\partial}{\partial z}C_{11}\frac{\partial}{\partial z}
\end{bmatrix}
\tag{2}
$$

where C_{11}, C_{12} and C_{44} are the elastic constants which also depend on z in the present system.

Next we introduce a new displacement vector $w(r, t)$ defined by

$$
u(r, t) \equiv \rho(z)^{-1/2}w(r, t). \tag{3}
$$

We see that w satisfies

$$
\ddot{w}(r, t) = \hat{H}w(r, t) + \rho(z)^{-1/2}f(r, t) \tag{4}
$$

where $\hat{H} \equiv \rho(z)^{-1/2}\hat{L}\rho(z)^{-1/2}$ is an Hermitian tensor operator, though $\hat{L}$ is not Hermitian. To solve equation (4) we introduce the retarded Green tensor $G_{ij}(r, r'; t) = G_{ij}(x_\parallel - x'_\parallel, z, z'; t)$ satisfying

$$
\left[\delta_{il}\frac{\partial^2}{\partial t^2} - \hat{H}_{il}\right]G_{lj}(r, r'; t - t') = \delta(r - r')\delta(t - t')\delta_{ij} \tag{5}
$$

with $G_{ij}(r, r'; t - t') = 0$ for $t < t'$. Then, the solution w should be given by

$$
w_i(r, t) = \int dr' \int dt' G_{ij}(x_\parallel - x'_\parallel, z, z'; t - t')\rho^{-1/2}(z')f_j(r', t'). \tag{6}
$$

To find the expression for the Green tensor G_{ij} we also introduce the Fourier transform $\mathcal{G}_{ij}$ of G_{ij} defined by

$$
\mathcal{G}_{ij}(k_\parallel, z, z'; \omega) = \int dx_\parallel \int_{-\infty}^{\infty} dt\, e^{-i(k_\parallel \cdot x_\parallel - \omega t)}G_{ij}(x_\parallel, z, z'; t) \tag{7}
$$

where $k = (k_\parallel, k_z) = (k_x, k_y, k_z)$ is the wavevector. This $\mathcal{G}_{ij}$ satisfies

$$
\left[\omega^2\delta_{il} + \hat{H}_{il}(k_\parallel, z)\right]\mathcal{G}_{lj}(k_\parallel, z, z'; \omega) = -\delta(z - z')\delta_{ij} \tag{8}
$$

where

$$
\hat{H}(k_\parallel, z) = \frac{1}{\sqrt{\rho(z)}}
$$

$$
\times
\begin{bmatrix}
C_{11}k_x^2 + C_{44}k_y^2 - \frac{\partial}{\partial z}C_{44}\frac{\partial}{\partial z} & (C_{12}+C_{44})k_xk_y & -ik_x[C_{12}\frac{\partial}{\partial z} + \frac{\partial}{\partial z}C_{44}] \\
(C_{44}+C_{12})k_xk_y & C_{44}k_x^2 + C_{11}k_y^2 - \frac{\partial}{\partial z}C_{44}\frac{\partial}{\partial z} & -ik_y[C_{12}\frac{\partial}{\partial z} + \frac{\partial}{\partial z}C_{44}] \\
-ik_x[C_{44}\frac{\partial}{\partial z} + \frac{\partial}{\partial z}C_{12}] & -ik_y[C_{44}\frac{\partial}{\partial z} + \frac{\partial}{\partial z}C_{12}] & C_{44}k_\parallel^2 - \frac{\partial}{\partial z}C_{11}\frac{\partial}{\partial z}
\end{bmatrix}
\frac{1}{\sqrt{\rho(z)}}
\tag{9}
$$

with $k_\parallel = |k_\parallel|$. Here we consider the eigenvalue equation

$$
\hat{H}(k_\parallel, z)Q_{k_\parallel}^{(\lambda)}(z) = \Omega_\lambda^2(k_\parallel)Q_{k_\parallel}^{(\lambda)}(z) \tag{10}
$$

where $\lambda = (k_z, n)$ consisting of the Bloch wave number k_z and the band index n discriminates the eigenvalues Ω_λ. The eigenvector $Q_{k_\parallel}^{(\lambda)}(z)$ satisfies the orthogonality relation

$$
\int dz\, \left[Q_{k_\parallel}^{(\lambda')}(z)\right]^* \cdot Q_{k_\parallel}^{(\lambda)}(z) = \delta_{\lambda'\lambda} \tag{11}
$$

and the completeness relation

$$
\sum_\lambda Q_{k_\parallel, i}^{(\lambda)}(z)\left[Q_{k_\parallel, j}^{(\lambda)}(z')\right]^* = \delta_{ij}\delta(z - z'). \tag{12}
$$

Now we can readily obtain

$$\mathcal{G}_{ij}(\boldsymbol{k}_\parallel, z, z'; \omega) = \sum_\lambda \frac{Q^{(\lambda)}_{\boldsymbol{k}_\parallel, i}(z)\,[Q^{(\lambda)}_{\boldsymbol{k}_\parallel, j}(z')]^*}{\Omega^2_\lambda(\boldsymbol{k}_\parallel) - (\omega + \mathrm{i}\varepsilon)^2} \tag{13}$$

where ε is an infinitesimal positive number that ensures the causality. The eigenvector $\boldsymbol{Q}^{(\lambda)}_{\boldsymbol{k}_\parallel}(z)$ has to satisfy the Floquet theorem required for a one-dimensional periodic system and takes the form

$$\boldsymbol{Q}^{(\lambda)}_{\boldsymbol{k}_\parallel}(z) = \frac{1}{\sqrt{L}} \sum_g \exp[\mathrm{i}\,(k_z + g)\,z]e^{(n)}_{kg} \tag{14}$$

where $g = 2\pi l/D$, $(l = 0, \pm 1, \pm 2, \ldots)$ is the reciprocal superlattice wave number, $D = d_A + d_B$ is the periodicity and $L = ND$ is the system size with N the number of the periodicity. The vector $e^{(n)}_{kg}$ is normalized as

$$\sum_g |e^{(n)}_{kg}|^2 = 1. \tag{15}$$

Noting the fact that $\sum_\lambda = (L/2\pi) \int_{-\pi/D}^{\pi/D} \mathrm{d}k_z \sum_n$, we have

$$G_{ij}\left(\boldsymbol{x}_\parallel - \boldsymbol{x}'_\parallel, z, z'; t\right) = \frac{1}{(2\pi)^4} \sum_n \sum_{gg'} \int \mathrm{d}\omega \int \mathrm{d}\boldsymbol{k}_\parallel \int_{-\pi/D}^{\pi/D} \mathrm{d}k_z$$

$$\times \frac{e^{(n)}_{kg,i}[e^{(n)}_{kg',j}]^*}{\Omega^2_{k_z,n}\left(\boldsymbol{k}_\parallel\right) - (\omega + \mathrm{i}\varepsilon)^2} e^{\mathrm{i}[\boldsymbol{k}_\parallel \cdot (\boldsymbol{x}_\parallel - \boldsymbol{x}'_\parallel) - \omega t]} e^{\mathrm{i}(k_z + g)z} e^{-\mathrm{i}(k_z + g')z'} \tag{16}$$

with $\Omega_\lambda = \Omega_{k_z, n}$. Here we assume the external harmonic force of the form $f_i(\boldsymbol{r}, t) = F\delta_{i,3}\delta(\boldsymbol{r})\exp(-\mathrm{i}\omega_0 t)$, with F a constant. Inserting equation (16) into (6) and using equation (3), we obtain the lattice displacement as

$$u_i(\boldsymbol{r}, t) = \frac{F\exp(-\mathrm{i}\omega_0 t)}{(2\pi)^3\sqrt{\rho(0)\rho(z)}} \sum_n \sum_{gg'} \int \mathrm{d}\boldsymbol{k}_\parallel \int_{-\pi/D}^{\pi/D} \mathrm{d}k_z \frac{e^{(n)}_{kg,i}[e^{(n)}_{kg',z}]^*}{\Omega^2_{k_z,n}(\boldsymbol{k}_\parallel) - (\omega_0 + \mathrm{i}\varepsilon)^2} e^{\mathrm{i}\boldsymbol{k}_\parallel \cdot \boldsymbol{x}_\parallel} e^{\mathrm{i}(k_z + g)z}. \tag{17}$$

The integral of equation (17) over wavevector $(\boldsymbol{k}_\parallel, k_z)$ can be converted to the integrals over the frequency Ω and over the surface of constant frequency defined by $\Omega_{k_z, n} = \Omega$. Thus, we obtain

$$u_i(\boldsymbol{r}, t) = \frac{F\exp(-\mathrm{i}\omega_0 t)}{2(2\pi)^3\omega_0\sqrt{\rho(0)\rho(z)}} \sum_n \sum_{gg'} \int \mathrm{d}\Omega \Bigg[\mathrm{Pr}\left(\frac{1}{\Omega - \omega_0} - \frac{1}{\Omega + \omega_0}\right)$$

$$+ \mathrm{i}\pi\left[\delta(\Omega - \omega_0) + \delta(\Omega + \omega_0)\right]\Bigg]$$

$$\times \int_{\Omega_{k_z,n}(\boldsymbol{k}_\parallel)=\Omega} \frac{\mathrm{d}S_k}{|\nabla_k\Omega_{k_z,n}(\boldsymbol{k}_\parallel)|} e^{(n)}_{kg,i}[e^{(n)}_{kg',z}]^* e^{\mathrm{i}\boldsymbol{k}_\parallel \cdot \boldsymbol{x}_\parallel} e^{\mathrm{i}(k_z + g)z} \tag{18}$$

where Pr means the principal part and $\mathrm{d}S_k$ is the surface element on the constant-frequency surface in the $\boldsymbol{k}$ space defined by $\Omega_{k_z, n} = \Omega$.

In the ultrasound transmission experiment done by Hauser *et al* [17, 18] with bulk solid samples, the immersion transducers are used to excite and receive the ultrasound. Hence, the acoustic signal measured should be the displacement amplitude corresponding to $|u_z|$ at the far side of the samples.
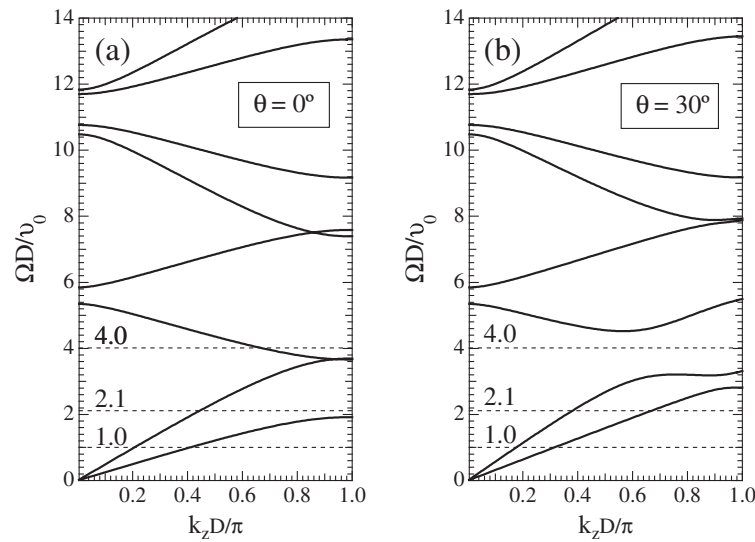
Figure 2. Dispersion relations of acoustic waves in the periodic (001) multilayer consisting of polycrystalline Al and polymer crystal bond layers, the layers being of equal thickness. The propagation direction (wavevector direction) are (a) $\theta = 0°$ (normal to the interfaces) and (b) $\theta = 30°$ rotated from the growth direction. Horizontal dashed lines indicate the frequencies $\Omega D/v_0 = 1.0, 2.1,$ and 4.0 for which the ultrasound images are calculated.

3. Numerical results

Here we remark that even if the constituent materials of the superlattice are elastically isotropic, two transverse modes of the acoustic waves are not degenerate for propagation oblique to the layer interfaces. This is because the superlattice has geometrical anisotropy arising from the layering structure. However, one of the transverse modes polarized parallel to the interfaces (the so-called shear mode with horizontal polarization (SH mode)) is decoupled from the other transverse mode as well as the longitudinal mode polarized in the sagittal plane (the plane containing the wavevector and perpendicular to the interfaces), which are coupled to each other. The latter coupled modes, called sagittal modes, are mathematically more complicated to study than the SH mode but physically more interesting. This is partly because the SH mode of the ultrasound does not induce lattice displacement perpendicular to the interfaces and hence is completely isotropic. However, the sagittal modes of the ultrasound are associated with lattice displacement perpendicular to the layer interfaces and hence exhibit propagation characteristics strongly dependent on the direction.

We also note that at low frequencies where the phonon wavelength becomes much longer than the unit period D of the superlattice, the displacement vectors of those two sagittal modes are well identified as parallel and perpendicular to the wavevector (precisely, they are quasi-longitudinal and quasi-transverse) and the slope of the dispersion curve with longitudinal polarization is steeper than the curve for transverse polarization (see figure 2). At higher frequencies we can also discriminate the branch of steeper slope from the other one and thus it should be convenient to label two sagittal modes as longitudinal (L) and transverse (T) according to their major polarizations, which usually coincide with the slope of the dispersion curves. This labelling, however, fails at anticrossing regions of the dispersion curves. Thus we will pay special attention to these regions so that there is no confusion in the identification of the branches.

Now we present the numerical results for a multilayer structure consisting of polycrystalline Al and polymer crystal bond (CB) layers. This means that the constituent layers are elastically isotropic, which is particularly suitable for seeing the effects of anisotropy arising from the one-dimensional periodic structure. We assume the same thickness for the constituent layers, i.e. $d_A = d_B$. The parameters assumed are the same as those used in the surface wave transmission experiments by Vines *et al* [19][1]. For sound velocities in the CB we assume $v_R/v_t = 0.93$ for the ratio of the velocities of the transverse and Rayleigh waves.

3.1. Dispersion relations

Figure 2 shows the dispersion relations $\Omega_\lambda (k_\parallel)$ versus k_z of acoustic waves propagating both normal ($\theta = 0°$) and oblique ($\theta = 30°$) to the layer interfaces of the superlattices. The angle θ denoted is defined by $\tan\theta = |k_\parallel|/k_z$. The number of reciprocal wave numbers g kept in the plane-wave expansion equation (10) for the calculation of the dispersion relations is 13 ($l = -6 \sim +6$). The relevance of this calculation has been confirmed by the fact that the dispersion curves do not change at all even if we further increase the number of plane waves in the expansion of equation (10). Compared with conventional semiconductor superlattices such as GaAs/AlAs, we see that the width of frequency gaps in this Al/polymer superlattice is larger because of the larger acoustic mismatch $Z_{Al}/Z_{CB} = \rho_{Al}v_{Al}^L/\rho_{CB}v_{CB}^L = 3.71$ (the corresponding ratio in the GaAs/AlAs superlattice is $Z_{GaAs}/Z_{AlAs} = 1.19$), where v^L is the longitudinal sound velocities of the constituent materials.

For oblique propagation the dispersion relations are more complicated due to the coupling of the longitudinal and transverse modes polarized in the sagittal plane, i.e. anticrossing of the dispersion curves occurs (see figure 2(b)). We also note that for oblique propagation $\theta \neq 0°$ the slope of the dispersion curve does not vanish at the zone boundary but is finite and proportional to $\tan\theta$. This is because for a given propagation angle θ the slope of the dispersion curve shown in this figure does not represent $\partial\Omega/\partial k_z$. Of course, $\partial\Omega/\partial k_z = 0$ at the zone boundary.

We choose three typical frequencies $\Omega D/v_0 = 1.0, 2.1$ and 4.0 ($v_0 = (C_{44,Al}/\rho_{Al})^{1/2} = v_{Al}^T = 3.09 \times 10^5$ cm s^{-1} is the transverse sound velocity in aluminium) to see the effects of Brillouin zone folding on the ultrasound images. The lowest frequency ($\Omega D/v_0 = 1$) is in the lowest frequency band for both L and T polarizations and the corresponding wavelength is much longer than the unit period D. The second one ($\Omega D/v_0 = 2.1$) is inside the lowest frequency gap of the T mode for normal propagation but this frequency is found inside the band of the T mode for propagation angles larger than $8.0°$ measured from the normal of the interfaces. The third one ($\Omega D/v_0 = 4.0$) is close to the frequency at which the dispersion curves of the L and folded T branches intersect at normal propagation. For a certain range of propagation angles ($\theta = 30°$, for instance, see figure 2(b)) this third frequency is found inside the intrazone frequency gap due to the intermode Bragg reflection between the L and T polarizations.

3.2. Slowness and group-velocity surfaces

$\Omega D/v_0 = 1.0$.   At this given frequency the wavelengths of both the L and T modes of acoustic waves are much longer than the unit period D and hence the ultrasound is essentially the same as in the bulk crystal with the mass density and elastic constants averaged over the constituent materials.

---

[1] The longitudinal sound velocities used are $v_{Al}^L = 6.37 \times 10^5$ cm s^{-1} for aluminium, and $v_{CB}^L = 4.69 \times 10^5$ cm s^{-1} for polymer (crystal bond), and the transverse sound velocities are $v_{Al}^T = 3.09 \times 10^5$ cm s^{-1} for aluminium, and $v_{CB}^T = 2.43 \times 10^5$ cm s^{-1} for polymer (crystal bond). The mass densities are $\rho_{Al} = 2.7$ g cm^{-3} for aluminium and $\rho_{CB} = 1.35$ g cm^{-3} for polymer (crystal bond).
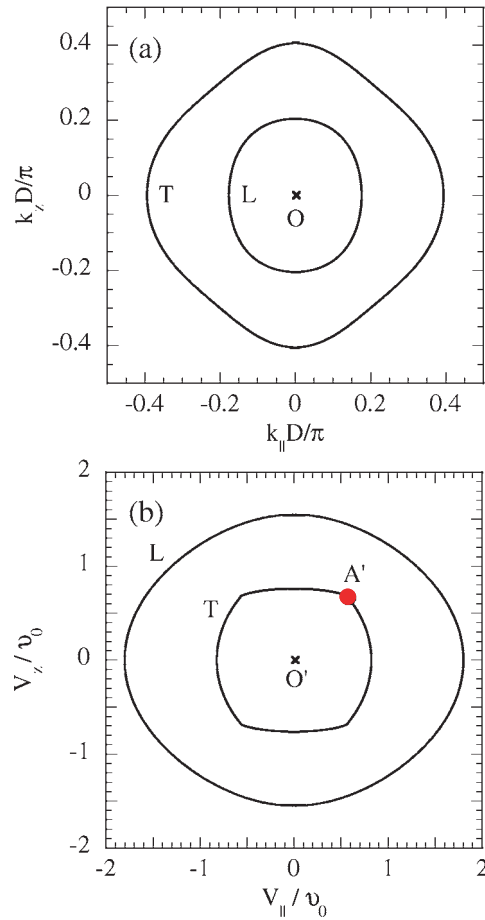
Figure 3. The (100) sections of (a) the slowness surfaces and (b) group-velocity surfaces of the longitudinal (L) and transverse (T) acoustic modes at $\Omega D/v_0 = 1.0$.

Accordingly, the constant-frequency surfaces (slowness surfaces) of two phonon modes in the wavevector space defined by $\Omega_\lambda (k_\parallel) = \Omega_0$, with Ω_0 a given constant, are entirely located inside the first Brillouin zone. The sections of the slowness surfaces in the $k_\parallel$–k_z plane and the corresponding sections of the group-velocity surface in the $V_\parallel$–V_z plane (in the real space) are shown in figures 3(a) and (b) respectively. In spite of the fact that each constituent material exhibits elastic isotropy, the composite layering structure is anisotropic and hence the shapes of the slowness curves are deformed from circles. Specifically, the slowness curve of the T mode is approximately flat for a certain range of propagation directions (over $26°$–$60°$). Because the direction of the group velocity is determined by the outward normal of the slowness surface, this leads to the accumulation of the group-velocity directions around the point A′ shown in figure 3(b). The ultrasound intensities are thus predicted to be enhanced along these directions.

$\Omega D/v_0 = 2.1$. The sections of the slowness surfaces in the $k_\parallel$–k_z plane and the corresponding sections of the group-velocity surface in the $V_\parallel$–V_z plane are shown in figures 4(a) and (b) respectively. The structures of both slowness and group-velocity curves are a bit more complicated than those of the previous cases due to the opening of the forbidden gaps at
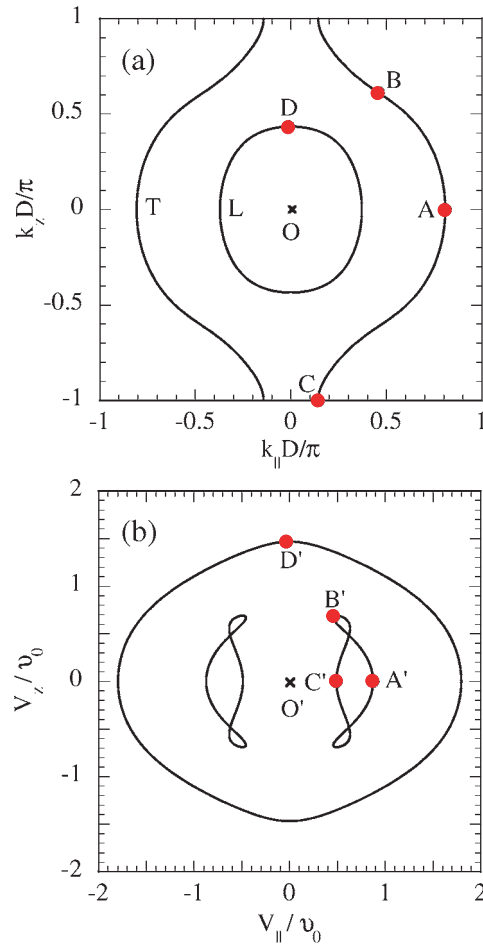
Figure 4. The (100) sections of (a) the slowness surfaces and (b) group-velocity surfaces of the longitudinal (L) and transverse (T) acoustic modes at $\Omega D/v_0 = 2.1$. The point labelled B is the inflection point with vanishing curvature. The points labelled A–D on the slowness curves correspond to the points labelled A'–D' respectively on the group-velocity curves.

the zone boundaries $k_z D/\pi = \pm 1$. At this frequency certain portions of the slowness curve of the T branch (near $k_\parallel = 0$, or at the normal propagation) is removed from the first Brillouin zone (no branch folded back to the first Brillouin zone exists).

Here it should be noted that the slowness curves intersect the boundaries of the first Brillouin zone at a right angle. So, at the intersecting points (point C, for example) the z component of the normal vector of the curves vanishes, or $\partial\Omega/\partial k_z = V_z = 0$, and no energy propagation is allowed along the growth direction of the superlattice. This restriction deforms the slowness curves considerably near the zone boundary and the regions of negative curvature are produced in addition to the portions of positive curvature. Thus the inflection points (B and its equivalent points) separate the sections of positive and negative curvatures of the T mode slowness curves.

The corresponding group-velocity curves of the T mode are located separately in the regions with positive and negative $V_\parallel$ components and no energy transport is allowed in the direction near the V_z-axis. As a consequence T-mode caustics (the direction $\overrightarrow{O'B'}$ and its
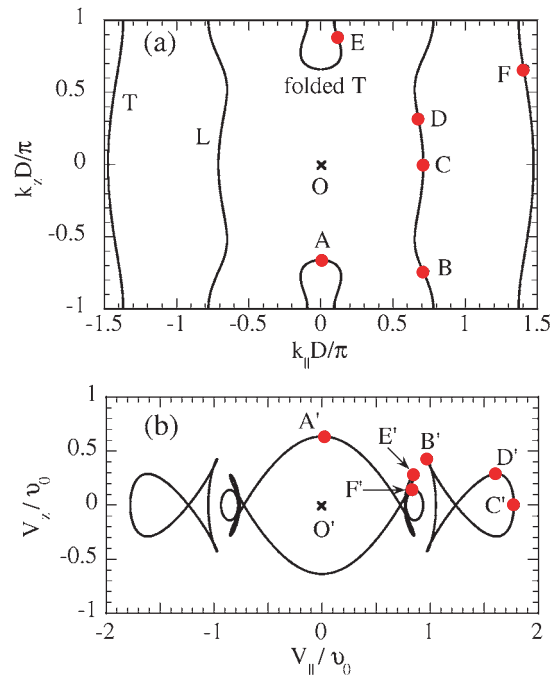
Figure 5. The (100) sections of (a) the slowness surfaces and (b) group-velocity surfaces of the longitudinal (L) and transverse (T) acoustic modes at $\Omega D/v_0 = 4.0$. The points labelled B, D, E, F in (a) are the inflection points with vanishing curvatures. The points labelled A–F on the slowness curves correspond to the points labelled A′–F′ respectively on the group-velocity curves.

equivalent directions in figure 4(b)) appear corresponding to the inflection point B and its equivalent points of the slowness curves and the T-mode group-velocity curves at this frequency are multiply connected. In contrast, the group-velocity curve of the L mode has an oval shape and no notable features are seen.

$\Omega D/v_0 = 4.0$.   The $k_\parallel$–k_z sections of the slowness and the corresponding group-velocity curves are shown in figures 5(a) and (b) respectively. The structures of the slowness curves are quite different from those in the low-frequency region and, at a glance, it is hard to identify which curve belongs to either the L or the T mode. A close examination reveals that the slowness curves existing near the zone boundaries $k_z D = \pm\pi$ and $k_\parallel = 0$ are those of the T mode folded back to the first zone. Also those vertical curves closer to the origin O are for the L mode and the ones located further from the origin are the for the T mode. On these curves there exist several inflection points, marked B, D, E, F, and their equivalent points not explicitly indicated.

Compared with those of the previous cases the corresponding group-velocity curves are much more complicated. The group-velocity curves corresponding to the outermost slowness curves (of the T mode) shown in figure 5(a) are the small vertical ovals attached to the curves of another T mode surrounding the origin O′ of this diagram. The group-velocity curves located outside these T-mode curves are those of the L mode with larger group velocity. All these group-velocity curves are folded at B′, D′, E′ and F′ originating from the inflection points B, D, E and F respectively of the slowness curves. The directions of the vectors $\overrightarrow{O'B'}$–$\overrightarrow{O'F'}$ define the caustics along which the ultrasound intensity diverges in the ray picture.
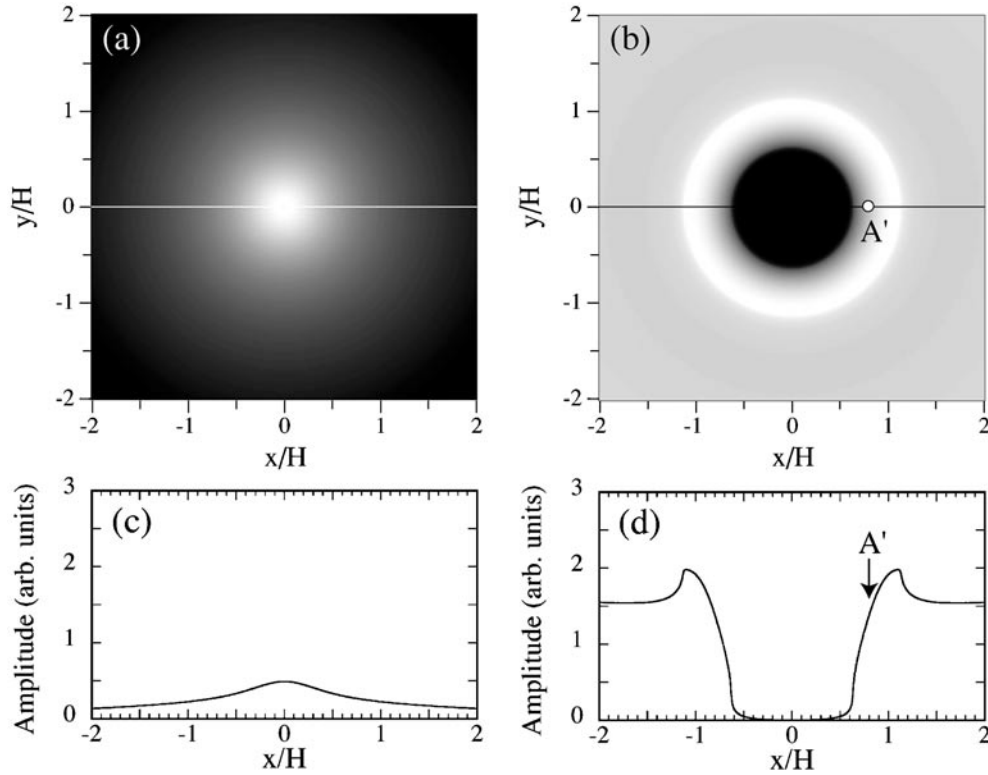
Figure 6. The amplitude $|u_z|$ and its images in the $x-y$ plane at $\Omega D/v_0 = 1.0..$ (a) L-mode image. (b) T-mode image. (c) Ultrasound amplitude versus the propagation angle of the L mode corresponding to (a). (d) Ultrasound amplitude versus propagation angle of the T mode corresponding to (b). The brightness measures the relative phonon intensity. The direction labelled A′ corresponds to the point A′ on the group-velocity curve of figure 2(b).

3.3. Ultrasound images

The amplitude $|u_z|$ and its images at those three frequencies in the $x-y$ plane (parallel to the layer interfaces) are shown in figures 6–8. The distance H between the emitter and receiver of the ultrasound is assumed to be 20 times the unit period, i.e. $H/D = 20$. These images span $-2 < \tan\Theta < 2$ (for figure 8, $-6 < \tan\Theta < 6$) in both the x and y directions, where Θ is the polar angle measured from the z-axis. Dark and light shadings correspond to small and large ultrasound amplitudes. It should be noted that in the $x-y$ plane the system is elastically isotropic and hence the images are completely circular.

$\Omega D/v_0 = 1.0.$ The results at this frequency in the $x-y$ plane are shown in figures 6(a) and (b). We see that the L mode focuses rather gently in the the growth direction $\tan\Theta = 0$. In contrast, the T-mode amplitude in this direction is very small because u_z of the T mode vanishes in the growth direction. However, the T-mode amplitude has a peak in the A′ direction ($\Theta = 42.2°$) corresponding to the direction normal to the flat region of the slowness surface. This enhanced amplitude is due to so-called 'precursor' effects, that is, if the frequency or other parameters change a bit, the slowness surface will be deformed to give a concave region, which leads to the folding of the group-velocity surface and the sharp enhancement of the ultrasound
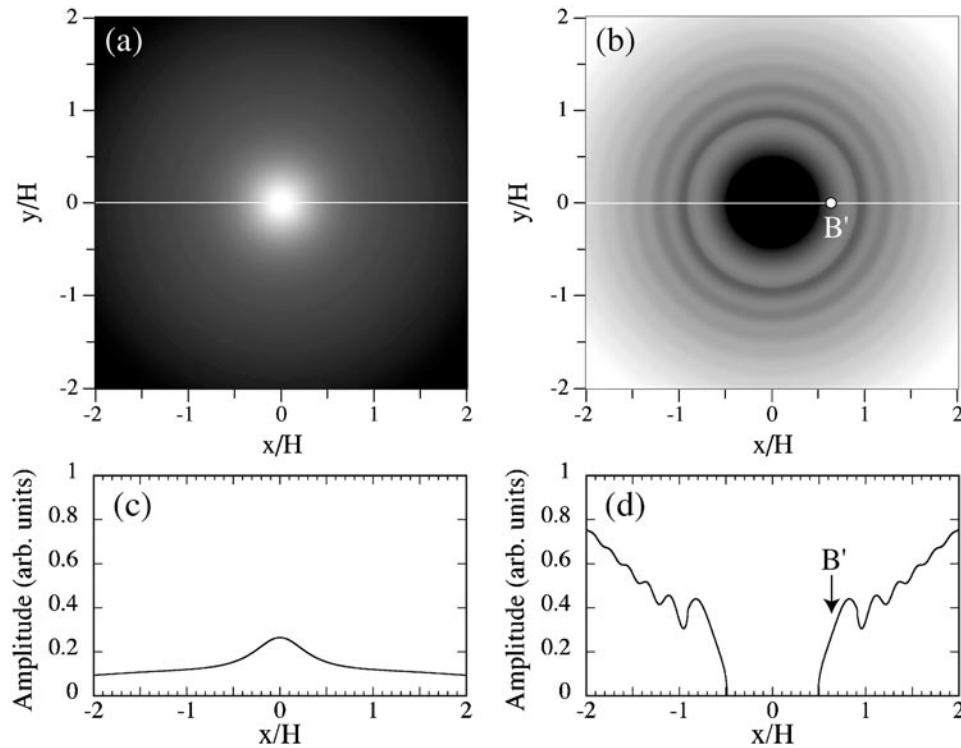
Figure 7. The amplitude $|u_z|$ and its images in the x–y plane at $\Omega D/v_0 = 2.1$. (a) L-mode image. (b) T-mode image. (c) Ultrasound amplitude versus propagation angle of the L mode corresponding to (a). (d) Ultrasound amplitude versus propagation angle of the T mode corresponding to (b). The direction labelled B′ corresponds to the point B′ on the group-velocity curve of figure 3(b).

amplitude. At this frequency, however, the slowness curve does not have a concave region, so no overlapping group velocities occur in a given propagation direction. An important consequence of this fact is that the ultrasound amplitude does not show any interference effect at smaller propagation distances.

$\Omega D/v_0 = 2.1$.   The results at this frequency in the x–y plane are shown in figures 7(a) and (b). Compared with the results for $\Omega D/v_0 = 1$, no qualitative change is observed for the L mode. In contrast, in the image of the T mode we find fringes which represents the oscillations in the intensity versus propagation angle measured from the growth direction. These oscillations are due to the interference called internal diffraction. The origin of this interference is the folding of the group-velocity surface of the T mode. The overlapping of the group-velocity surfaces in a given direction causes the interference of the waves. There is no measurable amplitude at the centre of the image due to the Bragg reflection of the transverse ultrasound propagating in the direction near the normal of the layer interfaces.

$\Omega D/v_0 = 4.0$.   Finally, the results at this frequency in the x–y plane are shown in figures 8(a) and (b). At this frequency the group-velocity surface of the L mode is also folded and as a result the fringes in the transmitted ultrasound intensity due to internal diffraction are seen. Also we see the absence of an L mode transmitted at the centre of the images, which is caused by the internal gap due to intermode Bragg reflections from the L to the T modes.
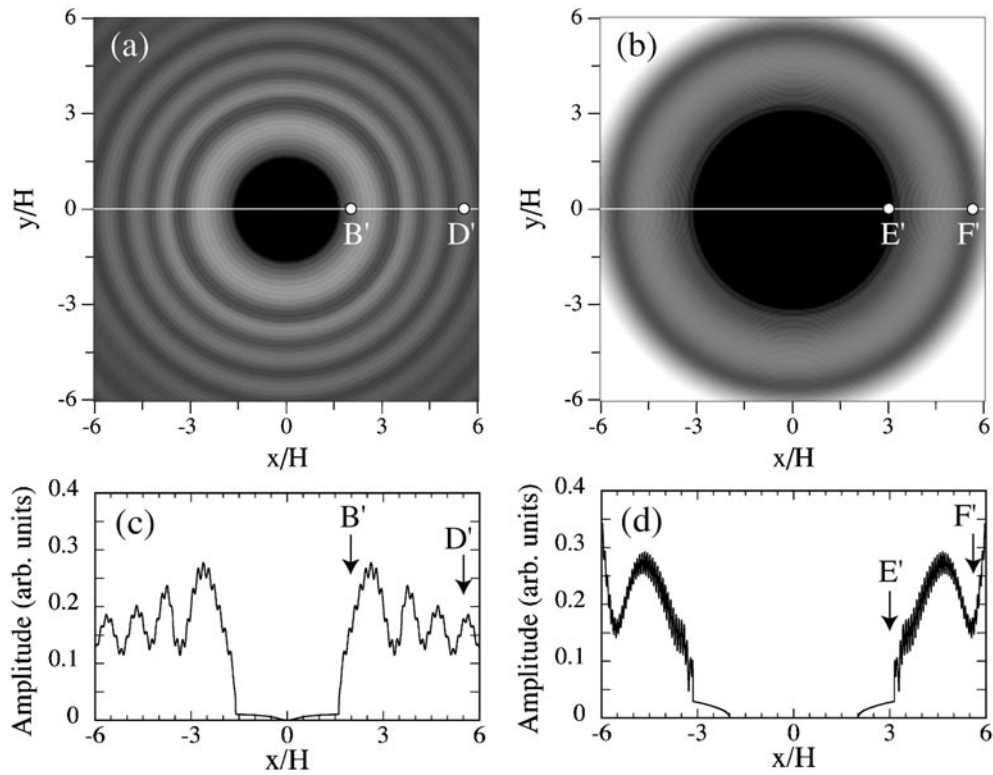
Figure 8. The amplitude $|u_z|$ and its images in the $x-y$ plane at $\Omega D/v_0 = 4.0$. (a) L-mode image. (b) T-mode image. (c) Ultrasound amplitude versus propagation angle of the L mode corresponding to (a). (d) Ultrasound amplitude versus propagation angle of the T mode corresponding to (b). The directions labelled B', D', E' and F' correspond to the points on the group-velocity curves of figure 4(b).

4. Concluding remarks

Based on a new mathematical formulation in which the lattice Green tensor is expanded in terms of the complete-orthogonal set of eigenfunctions of the perfect, periodic system satisfying the Bloch theorem, we have studied theoretically ultrasound focusing in an Al/polymer superlattice. We also considered the frequency region where the corresponding wavelength is comparable to the sample dimension and the effect of finite wavelength (the internal diffraction) becomes important.

In spite of the fact that the constituent layers assumed are elastically isotropic, the periodically stacked structure is itself anisotropic. Thus the predicted anisotropy in the ultrasound propagation is purely due to the layering structure of the superlattice and is seen as the propagation angle is rotated away from the growth axis of the superlattice. This anisotropic ultrasound propagation is enhanced by the Brillouin-zone folding characteristic of a periodic system and accordingly it is more conspicuous at frequencies closer to the zone centre, zone edge and internal gaps in the acoustic dispersion relations. The deformation of the slowness surfaces (and the resulting deformation of the group-velocity surfaces) results in the appearance of the caustics along which the acoustic intensity is focused sharply in the geometrical acoustic approximation.

For ultrasound propagation the folding of the group-velocity surfaces induces overlapping of acoustic fields in a given direction and hence causes interference between the amplitudes of the ultrasound with different wavevectors, leading to the existence of fringes in the images even for the longitudinal mode.

These new predictions for ultrasound focusing in superlattices should be verified by a mode-selective transmission experiment [19] with millimetre-thick periodic samples for which the wavelength of the ultrasound (with 1 MHz frequency range, for example) is comparable to the sample dimensions.

Acknowledgments

References

[1] Taylor B, Maris H and Elbaum C 1969 *Phys. Rev. Lett.* **23** 416
    Taylor B, Maris H and Elbaum C 1971 *Phys. Rev.* B **3** 1462
[2] Northrop G A and Wolfe J P 1985 *Nonequilibrium Phonon Dynamics* (New York: Plenum) ch 5
[3] Wolfe J P 1998 *Imaging Phonons* (Cambridge: Cambridge University Press)
[4] Baker A S Jr, Merz J L and Gossard A C 1978 *Phys. Rev.* B **17** 3181
[5] Colvard C, Merlin R, Klein M V and Gossard A C 1980 *Phys. Rev. Lett.* **45** 298
[6] Colvard C, Gant T A, Klein M V, Merlin R, Fischer R, Morkoc H and Gossard A C 1985 *Phys. Rev.* B **31** 2080
[7] Tamura S and Wolfe J P 1987 *Phys. Rev.* B **35** 2528
[8] Hurley D C, Tamura S, Wolfe J P and Morkoc H 1987 *Phys. Rev. Lett.* **58** 2446
[9] Tamura S, Hurley D C and Wolfe J P 1988 *Phys. Rev.* B **38** 1427
[10] Capinski W S and Maris H J 1996 *Physica* B **219–20** 699
[11] Capinski W S, Cardona M, Katzer D S, Maris H J, Ploog K and Ruf T 1999 *Physica* B **263–4** 530
[12] Capinski W S, Maris H J, Ruf T, Cardona M, Ploog K and Katzer D S 1999 *Phys. Rev.* B **59** 8105
[13] Hyldgaard P and Mahan H J 1997 *Phys. Rev.* B **56** 10 754
[14] Tamura S, Tanaka Y and Maris H J 1999 *Phys. Rev.* B **60** 2627
[15] Kiselev A A, Kim K W and Stroscio M A 2000 *Phys. Rev.* B **62** 6896
[16] Tanaka Y, Narita M and Tamura S 1998 *J. Phys.: Condens. Matter* **10** 8787
[17] Hauser M R, Weaver R L and Wolfe J P 1992 *Phys. Rev. Lett.* **68** 2604
[18] Weaver R L, Hauser M R and Wolfe J P 1992 *Z. Phys.* B **90** 27
[19] Vines R E, Wolfe J P and Every A G 1999 *Phys. Rev.* B **60** 11 871